Extensive microstructural quality control inside a machine tool using multiwavelength digital holography

T. Seyler[1*], M. Fratz[1], T. Beckmann[1], A. Bertz[1], D. Carl[1], V. Grün[2], R. Börret[2], F. Ströer[3], J. Seewig[3]
Fraunhofer Institute for Physical Measurement Techniques IPM,
Heidenhofstrasse 8, 79110 Freiburg, Germany;
Aalen University – Zentrum für optische Technologien (ZOT),
Beethovenstraße 1, 73430 Aalen, Germany;
University of Kaiserslautern, Institute for Measurement and Sensor-Technology (mts),
Gottlieb-Daimler-Straße, 67663 Kaiserslautern, Germany

*tobias.seyler@ipm.fraunhofer.de; phone +49 761 8857 176; fax +49 761 8857 224; www.ipm.fraunhofer.de

ABSTRACT

With state-of-the-art 3D measurement systems, short-wave structures such as tool marks cannot be resolved directly inside a machine tool chamber. Up to now, measurements had to be performed outside the machine tool. We present an interferometric sensor that carries out such measurements inside the machine tool, which saves time-consuming and expensive setup procedures.

Our sensor HoloCut uses digital holography as measurement principle. By the use of multiple wavelengths, we get a large unambiguous axial measurement range of up to 2 mm and achieve micron repeatability, even in the presence of laser speckles. With a lateral resolution of 7 µm across the entire 20 x 20 mm² field of view, both macro- and micro-structures (such as tool marks) are measured with an axial resolution of 1 µm. Consequently, this qualifies HoloCut for in-situ measurements and integration in a machine tool.

In this paper, the boundary conditions of integrating interferometers inside a machine tool are evaluated. Occurring vibrations and limited available space are particularly challenging constraints: The optical and mechanical design of HoloCut is introduced along with numerical correction algorithms: A piezo-stage setup is used to induce known displacements. Using these algorithms, measurements even with a closed-loop control of the machine tool head activated are demonstrated on a coin measurement. The use of HoloCut is motivated on the base of the daily operation of a 5-axis machine tool: We present an evaluation of an exemplary ISO 25178 parameter *Sq* using HoloCut measurements and compare those with reference, yet not inline-capable systems.

Keywords: Multiwavelength holography, Inline measurement, Quality control, Machine tool, Correlation, Deconvolution, ISO25178, 3d surface parameters

1. INTRODUCTION

Machining production faces increasing demands with regard to accuracy and persistent quality of manufactured parts. In order to meet these expectations and to minimize failure rates, 100% control is desirable[1]. However, random sampling is still common practice as current measurement systems are either very slow or lack in flexibility and cannot be integrated inline consequently.

Current machine tools mainly rely on tactile sensors to obtain a discrete estimate of the global shape. Besides the fact that these systems can only resolve long-wave structures, measurements are very time-consuming due to the tactile sensing of each individual point recorded.

For a more precise examination with regard to short-wavelength structures, manufactured parts must be transferred to separate measuring rooms. This is a very time-consuming task. Not only due to the transferring time needed but also since the parts must be set up for a potentially iterative process of revision both in the machine tool and on the measuring machine. Scanning tactile systems such as coordinate measuring machines are well-established to this day[2]. Competitive optical technologies[3] allow contact-free operation but are either limited in their application (reflecting parts for

Seyler, T.; Fratz, M.; Beckmann, T.; Bertz, A.; Carl, D.; Grün, V.; Börret, R.; Ströer, F.; Seewig, J., “Extensive microstructural quality control inside a machine tool using multiwavelength digital holography”, Speckle 2018: VII International Conference on Speckle Metrology, Proc. SPIE, Vol. 10834, Paper 108342B (1-13), 2018.

deflectometry), slower (whitelight interferometry) or have a significantly lower resolution (two orders of magnitude as for laser triangulation).

HoloCut is a miniaturized version of our existing sensor HoloTop[1] and works based on the principle of digital holography, which is an established technology for nondestructive testing in industrial applications[4–10]. It addresses the beforehand mentioned problems and can be used inside a machine tool to measure form and resolve short-wave irregularities with sub-µm resolution using 9 million data points per measurement at the same time. However, digital holography is very susceptible to vibrations and thus easily disturbed by machine tool environmental conditions.

We propose a method to predict information about the quality of single raw images of a measurement in terms of vibration superposition and present a solution to correct them if required: First, the effect of machine-induced vibrations of an in-machine tool measurement of a coin is presented. Solutions using correlation and deconvolution are compared for a piezo-stage setup and the latter applied to the previously introduced disturbed in-machine tool measurement.

Further, we motivate the application of HoloCut on the base of a surface evaluation according to ISO 25178 and compare it with reference, yet not inline-capable white light interferometry and confocal systems.

2. SETUP

2.1 Sensor design

The development of a sensor for use in a machine tool faces the challenge of harsh environmental conditions. Not only chips and oil contamination, but also limited space are challenges to be addressed. Therefore, the sensor was designed so that it does not extend more in height than a standard work tool and is lightweight enough to be mounted on the tool spindle. In order to comply with the limited space available inside a machine tool, the beam path is folded to a 3D layout as shown in a 3D view in Figure 1 (a).

Since interferometric measurement systems are particularly susceptible to vibrations and with respect to Section 2.2, the sensor is being mounted so that its center of gravity is in line with the spindle in order to minimize unwanted oscillations. Detailed information of the mechanical design is presented in a previous publication[11]. Figure 1 (b) shows the mechanical integration of HoloCut (blue) into a machine head (grey). A permanently installed stop-block (green) can be connected to the sensor's torque bracket (violet) to eliminate turning motions induced by the close-loop control of the machine head. Until now, this connection must be applied manually.

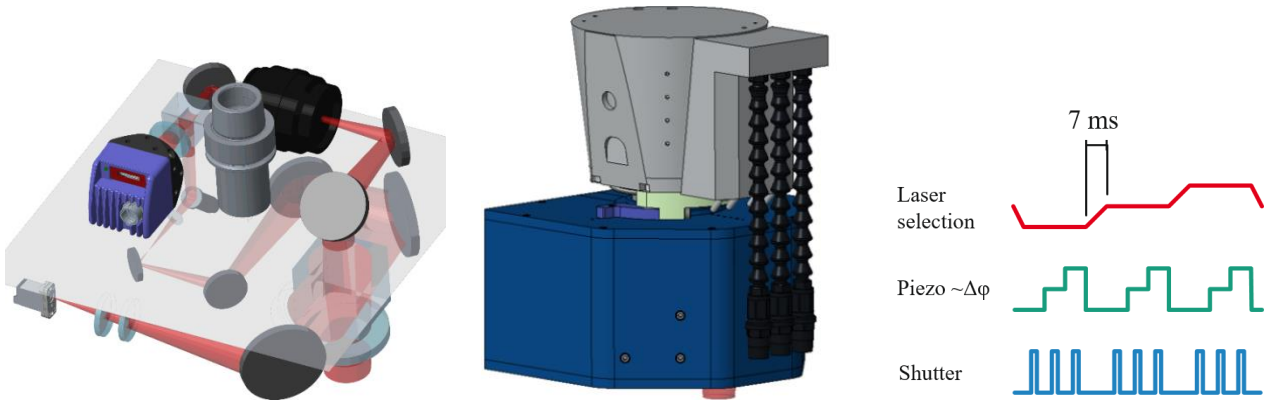

Figure 1. (a) HoloCut sensor design: 3D layout of beam path including separation plane with reference beam guidance on the bottom plane and object beam on the top plane. (b) Schematic integration of HoloCut (blue) into a machine head (grey). A permanently installed stop-block (green) is connected to the sensor's torque bracket (violet) manually with a screw. (c) Data acquisition time series using three lasers and three piezo steps for temporal phase shifting. In total, nine camera images are acquired.

With its small dimensions of 235 mm x 140 mm x 215 mm (W x H x D) and a sealed design, all mechanical challenges are addressed, which were identified previously. A measurement field of up to 20 mm x 20 mm combined with a lateral sampling of less than 7 µm (using more than 9 million measurement points per measurement) as well as an axial resolution

and repeatability of less than 1 µm are measuring specifications, which were realized. A laser system, consisting of multiple three fiber-coupled grating-stabilized diode lasers feeds a fiberswitch. Only one wavelength is present in the sensor at the same time. Measuring intervals of less than one second are achieved, making the sensor suitable for inline inspection. Figure 3 (c) shows the measurement data acquisition time series for a three laser setup at three phase steps including nine raw images. An exposure time of 1 ms was used for all evaluations in this paper.

2.2 Machine-tool environment

Figure 1 shows a schematic integration of our sensor into a standard 5-axis machine tool. Using all available axes, the sensor is capable of investigating even complex work piece geometries. In addition to the motion axes, machine tools have a spindle axes which is used for mounting the sensor. However, since most machine tools are not designed to block the rotational position of a work tool, the axis is continuously controlled by a closed-loop circuit and thus always exposed to very small movements. This disturbing movement is indicated in Figure 1 as an orange arrow.

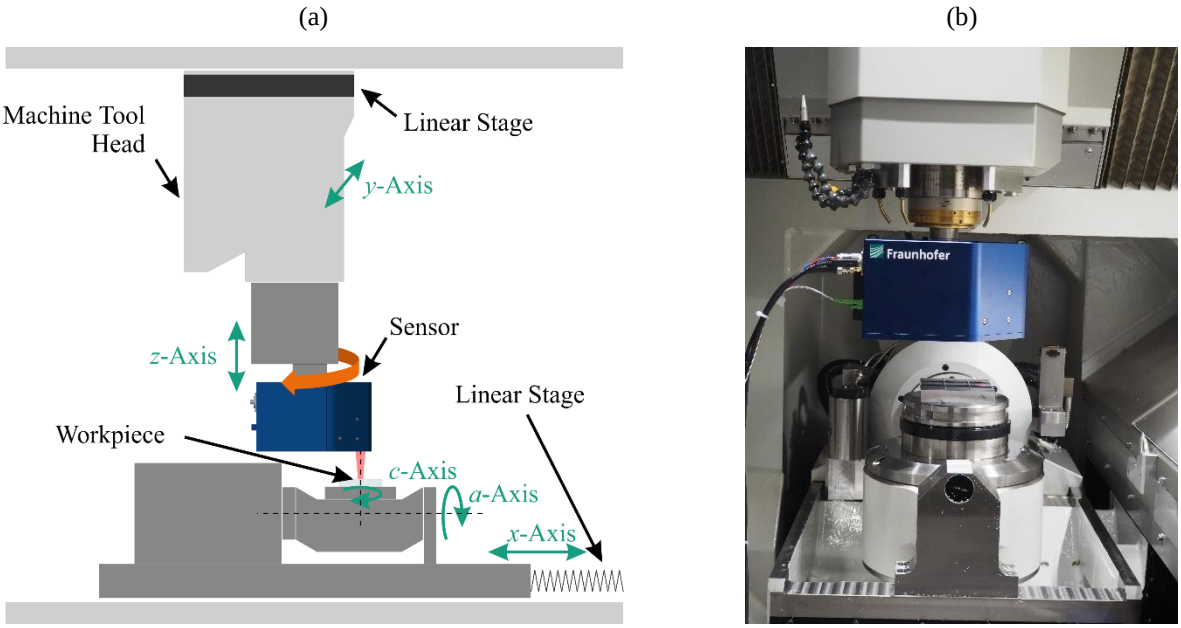

Figure 2. (a) schematic integration of HoloCut measuring a work-piece inside a standard 5-axis machine tool. The motion axis of the machine tool head closed-loop control is indicated in orange, (b) Photograph of HoloCut inside 5-axis milling machine.

2.3 Laboratory environment using piezo x-y-stage

Figure 3 (a) schematically shows the experimental setup used for algorithm development and comparison presented in Section 4.1. HoloCut is mounted on a height-adjustable column. An open-loop *x*-*y*-piezo underneath the sensor is used to initiate 20 defined displacements of half the pixel size (Δx = 3.3 µm) of the sensor. A last measurement was recorded at the starting position. The evaluations in this paper only contain displacements in *x*-direction.

A photograph of the experimental setup including sensor, piezo, a coin and a green laser system is shown in Figure 3 (b). However, since the algorithm is not limited to a certain wavelength, investigations with green and red lasers have been conducted. A red laser system with three lasers (λ_0 = 637.949 nm, λ_1 = 632.503 nm, λ_2 = 631.995 nm) has been used for all evaluations shown in this paper. Along with three phase steps φ_n = 3, one measurement consists of nine raw images.

Figure 3 (c) shows one image of this raw image stack with the total ROI (solid) and sub-ROIs (dashed) evaluated and the results median filtered in the algorithm later on. In the raw images, the measured coin is hardly visible, since the measurements have been taken 12 mm out of focus – the speckle share clearly dominates the image.

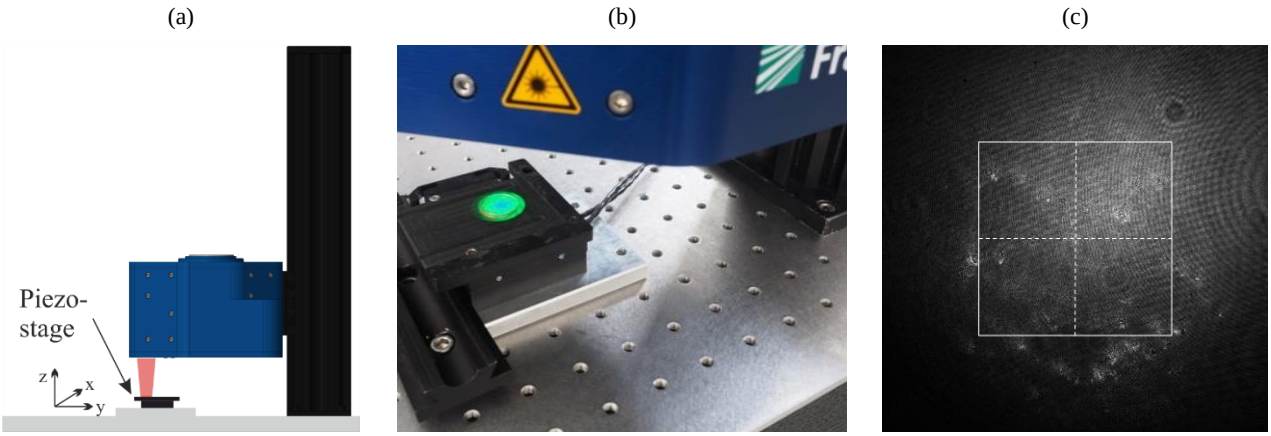

Figure 3. Experimental setup including (a) sketch including HoloCut sensor and a piezo stage, (b) photograph of the experimental setup, (c) one raw image out of nine total images within one measurement. The ROI (solid) and sub-ROIs (dashed) evaluated in the algorithm later on are indicated.

3. NUMERICAL RECONSTRUCTION

Surface evaluation from raw data is performed in four steps as illustrated in Figure 4:

1. Lateral vibration compensation
2. Temporal phase-shifting – determination of the global phase shifts between single images induced by the piezoactuator and calculation of the complex wave $C_\lambda(x,y)$ of each wavelength λ[12, 4]
3. Propagation of the complex wave $C_\lambda(x,y)$, filtering, calculation of wavefronts at synthetic wavelengths[12] and combination of artificial wavelengths[11]
4. Surface evaluation according to ISO 25178[13–15]

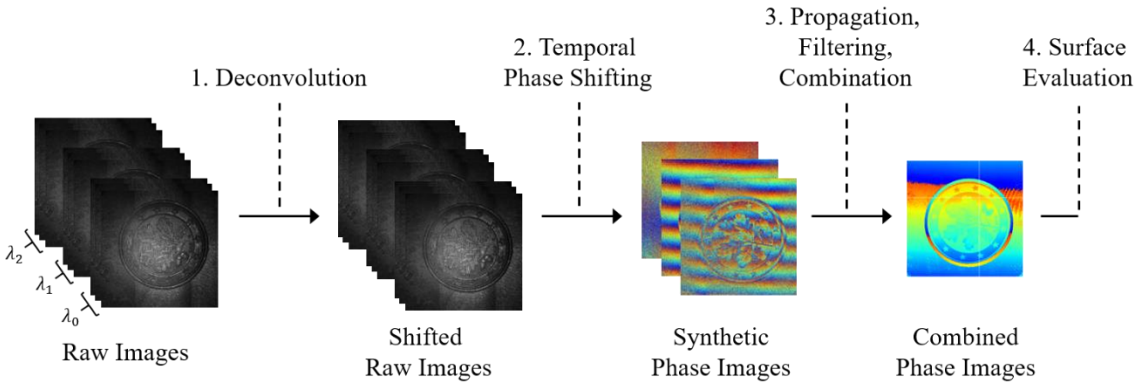

Figure 4. Data processing flow: Vibration compensation is applied on speckled raw images. Numerical reconstruction such as temporal phase shifting, propagation, filtering and combination of synthetic wavelengths follow subsequently.

In the following Sections 3.1 and 3.4, reconstruction steps 1 and step 4 will be described in detail. Step 1 proposes a method to predict information about the displacement of single raw images of a measurement during acquisition. In this process, the influence of steps 2 and 3 on the deconvolution result is taken into account. For step 4, the use of ISO 25178 for areal surface characterization is motivated and introduced.

3.1 Lateral vibration compensation

With multiwavelength digital holography, multiple wavelengths λ_i are fed successively into the sensor. The product of the number of wavelengths n_λ and the number of phase shifts n_φ at phase angle φ_n defines the number of raw images recorded

for one measurement. In the following, a total of nine images at three wavelengths and $n_\varphi = 3$ phase steps are recorded. Since multiple raw images are combined to complex holograms as shown in Figure 4, displacements of any kind disturb the evaluations and lead to strong artefacts in the measurement result. As previously introduced, the sensor is mounted onto a continuously position-controlled spindle and is thus always exposed to very small movements.

In signal theory, planar displacements are commonly tracked by the cross-correlation[16, 17]. However, on periodic structures such as tool marks, cross-correlation results in multiple local maxima.
In analogy to a 1D signal[18], lateral shifts of a 2D image can be generated by convolution of an input image with dirac impulse kernel. The reverse operation is called deconvolution and has proven to be very effective for this application. Both approaches are introduced and evaluated in the following.

3.2 Cross-Correlation

There are various commonly used cross-correlation C_{CC} criterions for correlating a reference image $f(x,y)$ with a mask or image section $g(x',y')$[16, 17]. In the space domain, the simplest approach is calculated as follows:

$$C_{CC} = \sum_{x'=m-r}^{m+r} \sum_{y'=n-r}^{n+r} [f(x,y)g(x',y')] \tag{1}$$

An image section $g(x',y')$ with radius r is moved across and multiplied with the reference image $f(x,y)$. On a reference image $I_{\text{ref}}(x,y)$ and a displaced image $I_{\text{displ}}(x,y)$, the operation can be written as

$$C_{CC} = I_{\text{ref}}(x,y) \otimes I_{\text{displ}}(x,y) \tag{2}$$

where $\otimes$ denotes the correlation operation.

Figure 5 illustrates the operation with two laterally shifted height maps of a milled surface. Since the height maps underlie a periodic structure, the correlation result C_{CC} reproduces this effect.

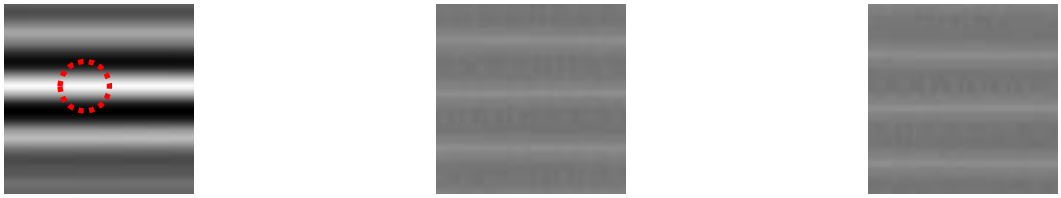

C_{CC} $I_{\text{ref}}(x,y)$ $I_{\text{displ}}(x,y)$

Figure 5. Correlation of two laterally shifted height maps of a milled surface.

Besides this periodic structure, a peak five pixels out of the center to the upper left shows the shift of the two images to each other. In spite of the periodicity, a maximum filter yields the desired lateral shift. For subpixel accuracy, additional preprocessing with subsequent evaluation of a symmetric region of interest (ROI) around the maximum is typically applied.

Performing the cross-correlation in the frequency domain, the correlation operation turns into a multiplication and reduces the number of calculations from $O(N^2)$ to $O(N \log_2 N)$. For this reason, cross-correlation is typically calculated in the frequency domain. For a recorded image $I_{\lambda_{\text{ref}},\varphi_{\text{ref}}}$ at wavelength λ and phase step φ, the cross-correlation in the frequency domain is calculated by multiplication of the Fourier transform of one image $I_{\lambda_{\text{ref}},\varphi_{\text{ref}}}$ with the complex conjugate Fourier transform of a second image $\overline{I_{\lambda_i,\varphi_k}}$.

$$T_{i,k} = DFT^{-1}\left\{DFT\{I_{\lambda_{\text{ref}},\varphi_{\text{ref}}}\} DFT\{\overline{I_{\lambda_i,\varphi_k}}\}\right\} \tag{3}$$

In order to improve the signal-to-noise ratio, the mean value is subtracted from this result and then normalized to the standard deviation.

3.3 Deconvolution

A displaced image I_{displ} can be shifted by one pixel by convolution with a transformation matrix T which is zero in every element but one next to the middle. Figure 6 shows this computation graphically. Transparent boxes in the illustration represent zeros, whereas black boxes represent ones. The resulting image I_{conv} was shifted by one pixel.

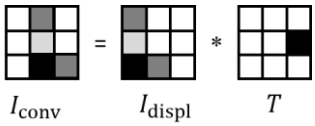

Figure 6. Shifting an image using convolution

With deconvolution, the opposite way is approached. By determining an unknown displacement matrix $T_{\lambda,\varphi}$ via deconvolution of a raw image in reference position $I_{\lambda_{\mathrm{ref}},\varphi_{\mathrm{ref}}}$ with a displaced raw image $I_{\lambda_i,\varphi_k,\mathrm{displ}}$. In analogy to the cross-correlation, a convolution in the time domain corresponds to a multiplication in the frequency domain. The deconvolution matrix $T_{i,k}$ for a wavelength λ_i and a phase step φ_k is calculated by

$$T_{i,k} = DFT^{-1}\left\{\frac{DFT\{I_{\lambda_{\mathrm{ref}},\varphi_{\mathrm{ref}}}\}}{DFT\{I_{\lambda_i,\varphi_k}\}}\right\} \tag{5}$$

with $i \in n_\lambda$ and $k \in n_\varphi$. Figure 7 shows the output for this calculation and the images from above.

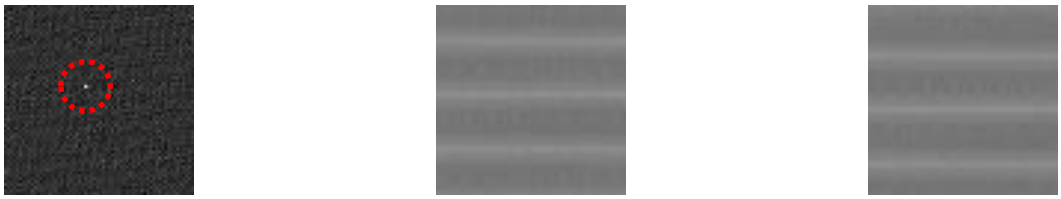

C_{CC} $I_{\mathrm{ref}}(x,y)$ $I_{\mathrm{displ}}(x,y)$

Figure 7. Correlation of two laterally shifted height maps of a milled surface.

As previously traced, a clear maximum five pixels out of the center to the upper left returns the displacement of both images to each other. However, with this approach the periodic basic structure is suppressed. A subpixel evaluation can therefore be carried out directly on this image. The center of gravity is calculated within an ROI with a radius of five pixels around the maximum filter output.

For $i, n = 0$, the deconvolution of two identic images is calculated and results in a transformation matrix with perfectly centered peak of the amplitude one. Since the deconvolution matrix $T_{i,k}$ perfectly transforms two images into each other, a filter in the Fourier domain is applied, which removes image differences independent of the displacement such as noise or phase induced information. Unwanted transformation information due to different laser wavelengths and phase steps can be mainly found in the higher frequencies and thus off-center in the Fourier space. Thus, high frequency components in the discrete Fourier transform are being set to zero, which is equivalent to applying a low-pass filter in the spatial domain.

$$T_{i,k} \rightarrow \widetilde{T_{i,k}} \tag{7}$$

The so processed transformation matrix $\widetilde{T_{i,k}}$ is then applied to the displaced image $I_{\lambda_i,\varphi_k,\mathrm{displ}}$ in order to move it to the position of the reference image $I_{\lambda_{\mathrm{ref}},\varphi_{\mathrm{ref}}}$:

$$I_{\lambda_i,\varphi_k,\mathrm{conv}} = DFT^{-1}\left\{DFT\{\widetilde{T_{i,k}}\} \cdot DFT\{I_{\lambda_i,\varphi_k,\mathrm{displ}}\}\right\} \tag{8}$$

In Section 4.1 and for comparison of the decorrelation and the deconvolution approach, the lateral displacement of the original input image is calculated from the transformation matrix $\widetilde{T_{i,k}}$. Maximum filter and center of gravity calculations are evaluated.

3.4 Surface evaluation according to ISO 25178

Common procedure in the industry, when characterizing a workpiece using surface roughness parameters, is to extract 2D profile sections $Z(x)$. Unfortunately, this operation can result in a loss of information. Especially random structures cannot be characterized sufficiently using only a 2D profile. The calculation of 2D surface roughness parameters is described in various standards such as ISO 3274, ISO 11562, ISO 13565-1, ISO 4287, ISO 4288 and ISO 1365-2.

The HoloCut sensor offers the possibility to evaluate the measured surface topography over a wide area, enabling a function- and structure-oriented 3D evaluation of the surface $Z(x, y)$ according to the EN ISO 25178 series[13–15]. Among other surface texture definitions, the 2D parameters *Ra*, *Rq* and *Rz* established in practice were transferred to their corresponding 3D parameters *Sa*, *Sq* and *Sz*.

In a first processing step, the standard provides preparation of the measured data to be evaluated with the following filters[14]:

- F-operator: removes the nominal shape,
- S-Filter: removes high-frequency sensor noise using a low-pass filter,
- L-Filter: removes low-frequency shape deviations and ripples using high-pass filters

Subsequently, different parameters are obtained which are divided into different categories[14]:

1. Height parameters: *Sq, Ssk, Sku, Sp, Sv, Sz, Sa*
2. Spatial parameters: *Sal, Str, Std*
3. Hybrid parameters: *Sdq, Sdr*
4. Functions and related parameters*: Smr, Sdc, Sxp, Vm, Vv, Vmp, Vmc, Vvc, Vvv*
5. Parameters related to segmentation: *Spd, Spc, S10z, S5p, S5v, Sda(c), Sha(c), Sdv(c), Shv(c)*

Most of these parameters were implemented and are used to characterize milling surfaces. The results in this paper are exemplified by the parameter Sq which is defined as follows[14]

$$Sq = \sqrt{{}^{1}/_{A} \iint_{A} Z^2(x, y)\ \mathrm{dxdy}} \tag{9}$$

where Z represents the height of a surface for each pixel (x, y). The multiwavelength digital holography sensor HoloCut, a Zygo white light interferometer and a NanoFocus confocal microscope are used for this evaluation.

4. RESULTS

4.1 Lateral vibration Compensation

Using temporal phase shifting, three images are combined and hence have to be laterally matched for step 2 and step 3. There are several ways to apply the vibration compensation algorithms: For the temporal phase shifting with φ_n = 3 phase steps, three holograms can be calculated and thus combined to one complex hologram. This allows vibration compensation on the raw images of a single laser with subsequent vibration compensation on the synthetic holograms or vibration compensation over all raw images instead.

In the following, only the latter option is applied. First, correlation is compared to deconvolution using the piezo setup. The deconvolution algorithm is then applied to a disturbed coin measurement, recorded inside the machine tool.

4.2 Comparison of Cross-Correlation and Deconvolution using piezo x-y-stage

Figure 8 shows a comparison of the correlation approach with the deconvolution approach for maximum filter and center of gravity evaluation. The couple $I_{\lambda_0,\varphi_0}, I_{\lambda_0,\varphi_1}$ is exemplarily shown here comparing same wavelengths at different phase step.

Figure 8 (a) shows a very consistent progression for the Δx output of all approaches. Except for the maximum filtered deconvolution, all values are close to the expected zero. In Figure 8 (b), Δy shows a constant offset to zero of the correlation output compared to the deconvolution output being close to zero. With the introduction of physical displacements using the piezo stage, the progression of Δx shows a linearly increasing output as shown in Figure 8 (c). Whereas the correlation

output clearly fluctuates around the expected linear increasing reference line, deconvolution shows a visibly lower deviation. Furthermore, the influence of the centre of gravity calculation does not seem to have a positive influence on the correlation, whereas the deviations of the deconvolution from the reference decrease. Figure 8 (d) shows the Δy output with the Δx piezo displacements and shows a similar course for the deconvolution as Figure 8 (c).

$I_{\lambda_0,\varphi_0}, I_{\lambda_0,\varphi_1}$ $I_{\lambda_0,\varphi_0}, I_{\lambda_0,\varphi_1}$

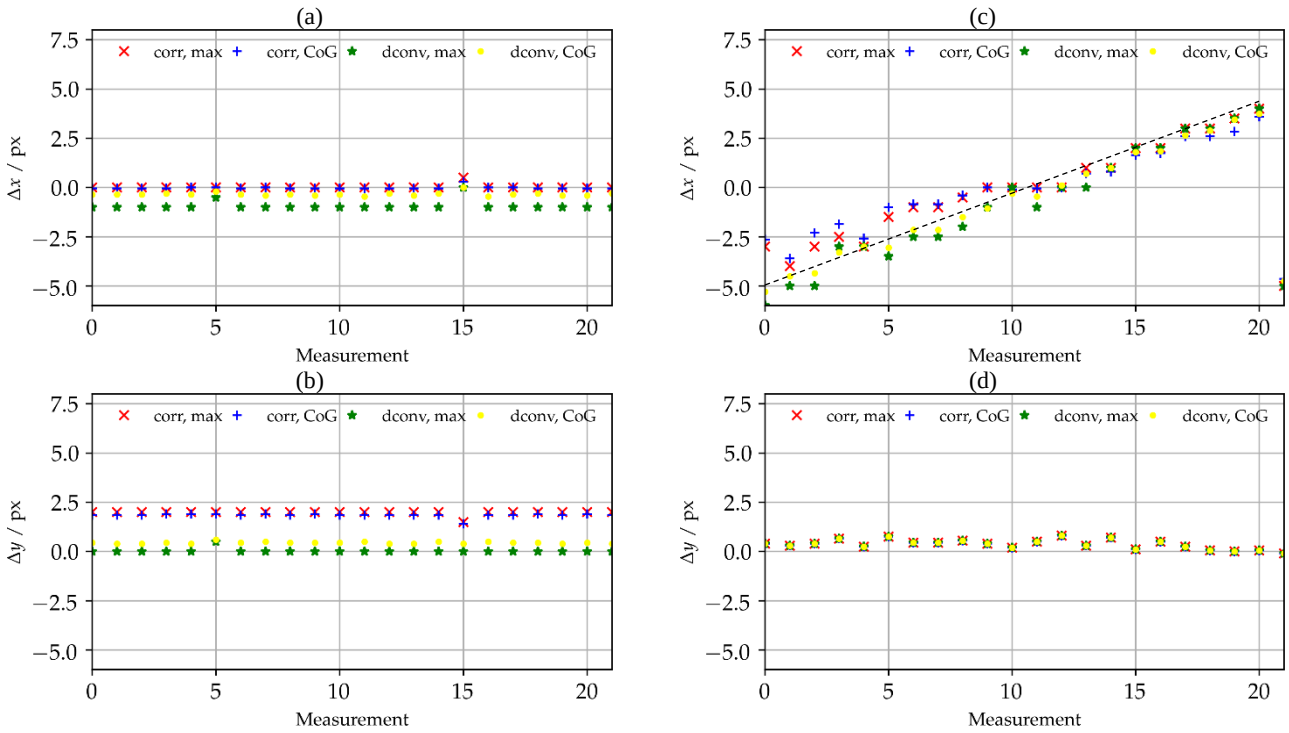

Figure 8. Comparison of correlation and deconvolution on stationary measurements and linearly increasing displaced measurements: (a) Δx output without external displacement, (b) Δy output without external displacement, (c) Δx output with piezo-induced displacement, (d) Δy output with piezo-induced displacement

With the deconvolution approach, piezo displacements could be reproduced with higher accuracy. In addition, the filtered deconvolution output $\widetilde{T_{\iota,k}}$ can be immediately applied to the displaced image.

With this algorithm, only lateral displacements can be detected and corrected. Axial vibrations cannot be detected. For our application inside the machine tool, the torsional vibration of the spindle axis is the main disturbance. It results only in lateral displacement and can thus be addressed by the algorithm. The rotational movement of the spindle can be interpreted as a homogenous displacement for this initial attempt.

4.3 Deconvolution on in-machine tool measurements

First, exemplary correlation and deconvolution outputs of the total ROI shown in Figure 3 (c) are presented for a displaced coin measurement. The measurement has been recorded inside the machine tool with activated closed-loop control of the machine tool head.

All plots contain the center of the correlation/deconvolution results within a radius of ten pixels shown with the black dashed lines. A white cross marks the region of interest around the maximum with a radius of five pixels evaluated for the center of gravity as introduced in Section 3. Panel (a.*) shows the autocorrelation/deconvolution of the reference image for all further evaluations. Panel (b.*) compares I_{λ_0,φ_0} to a raw image of the same laser but a different phase step. In panel (c.*) the phase step was kept constant but the wavelength differs. Panel (d.*) is evaluated at a different wavelength and phase step.

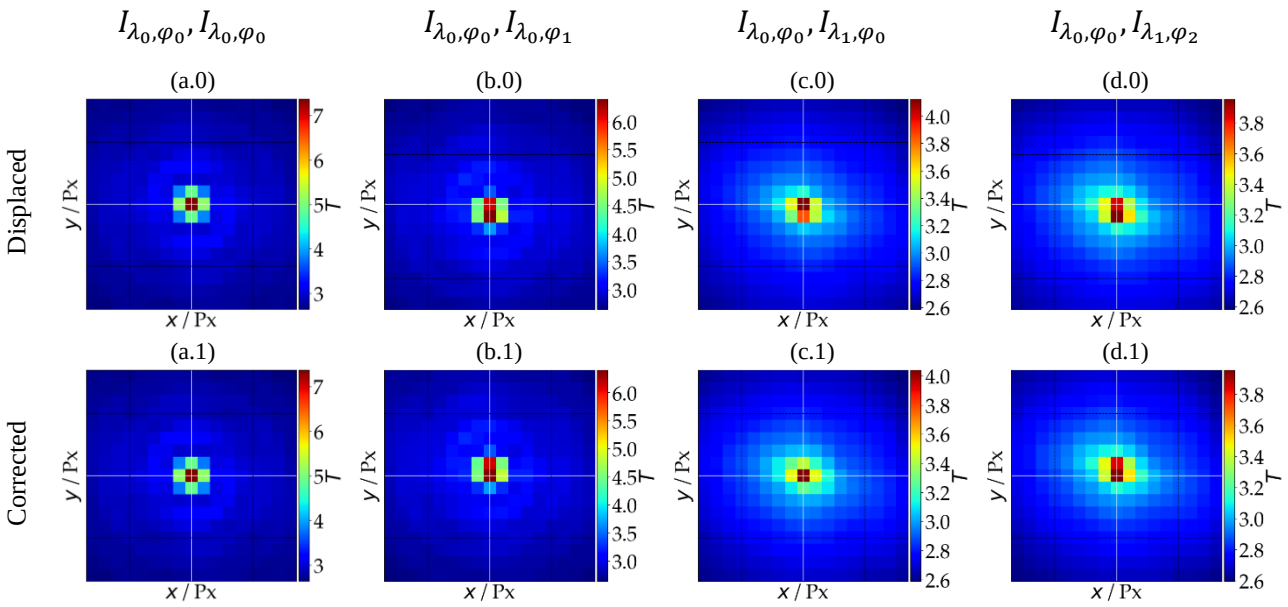

Figure 9. Correlation plots of displaced (*.0) and corrected (*.1) raw images to reference image I_{λ_0,φ_0} in frequency domain according to Table 1. With their maximum off-centered, corrections were applied to (b) and (d).

As expected, the autocorrelation in Figure 9 (a) shows a clear maximum in the middle of the matrix. The correlations in (9b.0), (9c.0) and (9d.0) show a slightly off-centered peak and are thus shifted in the subpixel range. The translation leads to a maximum in the center of (9b.1), (9c.1) and (9d.1). Despite the normalization, a low signal to noise ratio of the peak to its surrounding can be observed.

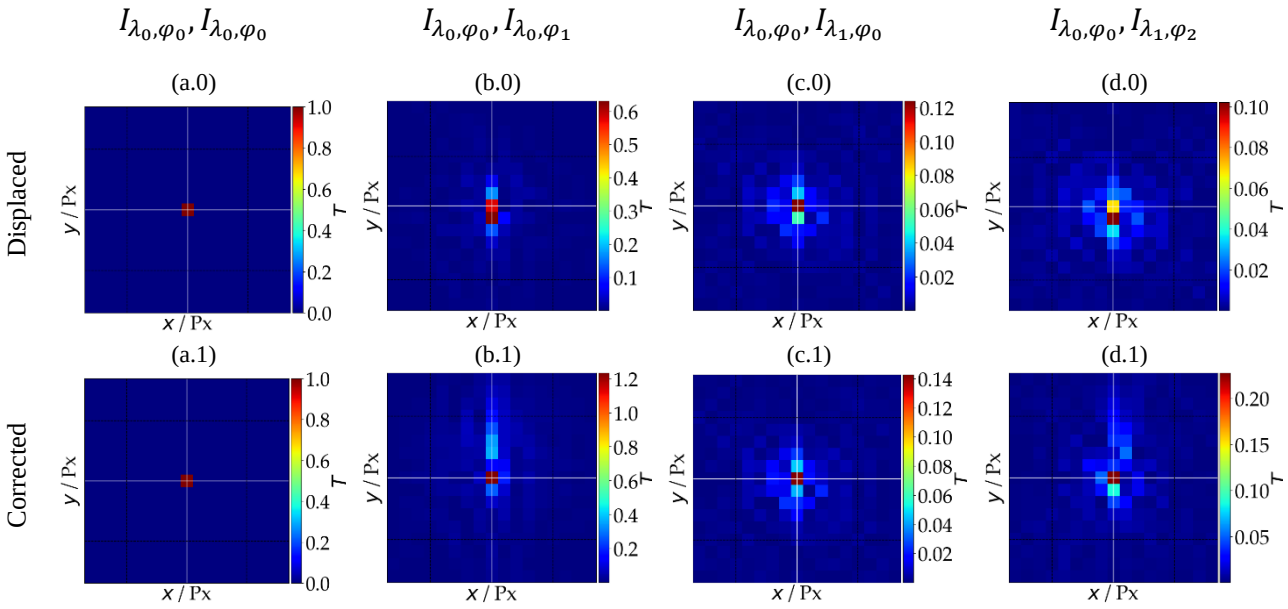

Figure 10. Deconvolution plots of displaced (*.0) and corrected (*.1) raw images to reference image I_{λ_0,φ_0} in frequency domain according to Table 1. With their maximum off-centered, corrections were applied to (b) and (d).

Deconvolution overcomes this drawback as shown in Figure 10. Clear peaks can be observed whereas the background of the ROI is close to zero. In analogy to the correlation plots, the autocorrelation in (10.0) shows a clear maximum in the middle of the matrix. The correlations in (10b.0), (10c.0) and (10d.0) show a slightly off-centered peak and are thus shifted in the subpixel range. The algorithm results in stronger peaks in the center of (10b.0), (10c.0) and (10d.0) as can be read

from the colorbars. With a significantly higher signal to noise ratio using the deconvolution approach without further processing, we see a clear advantage of this method.

Figure 11 shows the successive combination of synthetic wavelengths of this measurement on top of each other. Starting with the rough signal in panel (a), the largest synthetic wavelength does not show disturbances yet. With the application of the finer wavelength in panel (b), strong artefacts overlay the measurement result. The finest synthetic wavelength applied in panel (c) does not further improve or deteriorate this result. The implied white cross shows the reference point for synthetic hologram combination.

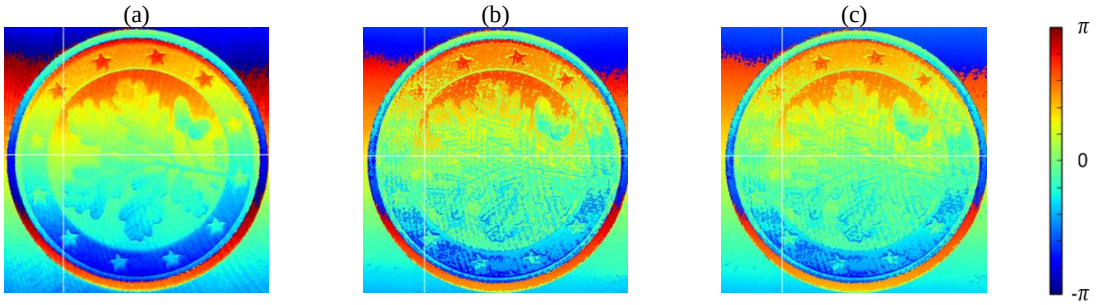

Figure 11. False color display on phase information of a coin without deconvolution algorithm: (a) rough signal, free of artefacts (b) after finer synthetic wavelength with strong artefacts (c) after finest synthetic wavelength with strong artefacts. A white cross indicates the reference point.

With the application of the for our application superior deconvolution approach the measurement is significantly improved. Four equal regions of interest across the whole image are processed to better compensate for the displacement. In this specific measurement, the algorithm does not affect the rough signal significantly as shown in Figure 12 (a). However, the finer synthetic wavelength in Figure 12 (b) is now applied without introducing strong artefacts. The same applies to the finest synthetic wavelength. The resulting image in Figure 12 (c) is almost free of artefacts. These observations coincide with the displacements of the raw images used to calculate the respective synthetic wavelengths.

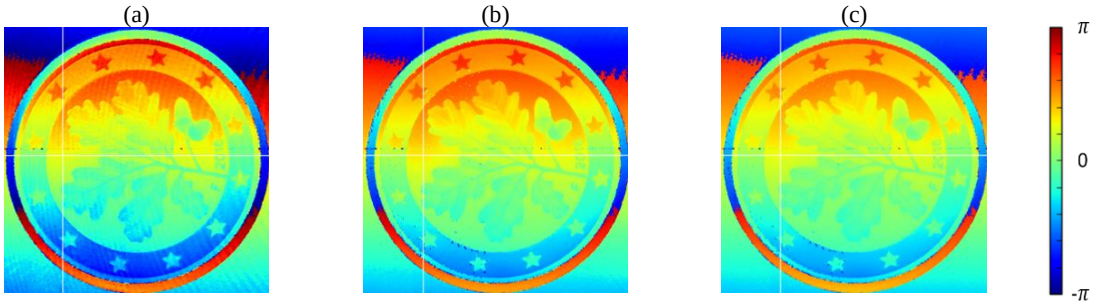

Figure 12. False color display on phase information of a coin deconvolution algorithm: (a) rough signal free of artefacts (b) after finer synthetic wavelength free of artefacts (c) finest synthetic wavelength free of artefacts. A white cross indicates the reference point.

Further improvements and more robust evaluation is expected for rotationally correct evaluation. Further maximum filters and center of gravity can be extended by a spline fit.

4.4 Evaluation of *Sq* as a surface parameter according to ISO 25178

In order to evaluate the measurement data quality of the holographic sensor for a milling surface, four aluminum samples F, G, H and J with 25 test fields each, were prepared as shown in Figure 13 (a). A Hitachi HECOB2060-PN ball-end milling cutter, with a tool diameter of 6 mm and 2 tool cutters, was used in climb milling with flood lubrication for all parts. Cutting speed was set to 14900 rpm, the feed rate to 3310 mm/min and the cutting depth to 0.2 mm. Milling parameters were kept constant between the samples. All four samples were produced at different intervals on consecutive days. In order to distribute the influence of unknown systematic errors (e.g. position-dependent positioning accuracy) over the entire workpiece, the machining sequence was partially randomized into columns.

To assess the data quality of the HoloCut sensor, the following reference sensors were compared:

Table 1 Comparison of sensors being part of the evaluation: Multiwavelength digital holography sensor HoloCut (HOLO), Zygo White light interferometer (WLI - reference), NanoFocus confocal microscope (CONF - reference)

	HoloCut	**Zygo NewView 100**	**NanoFocus µSurf Explorer**
Name	HOLO	WLI	CONF
Probing	optical	optical	optical
Single field of view / mm²	20 x 20	4.9 x 3.7	1.6 x 1.6
Stitched field of view / mm²	/	/	3.8 x 3.8
Measuring time / 20 mm²	< 500 ms	> 10 min	> 15 min
Lateral resolution / µm	6.65 µm	15 µm	3.13 µm
Axial resolution / µm	< 1 µm	0.1 nm	< 10 nm

With all three optical sensors, huge differences between the sample F and G compared to H and J are observed, even though produced with the same milling parameters. HoloCut data for single measurements of a good part (left) and a poor part (right) are illustrated as a projection onto the photograph in Figure 13. A detailed section of one measurement is depicted in Figure 13 (b) and (c), respectively. In both detail views, milling traces are clearly resolved by the sensor. At a closer look, there is a huge difference in the depth of the cutting paths. For the good parts F and G, shown in panel (b), all cutting paths range from -3 µm to +3 µm. On the other hand three times the height expansion is present for the poor parts H and J.

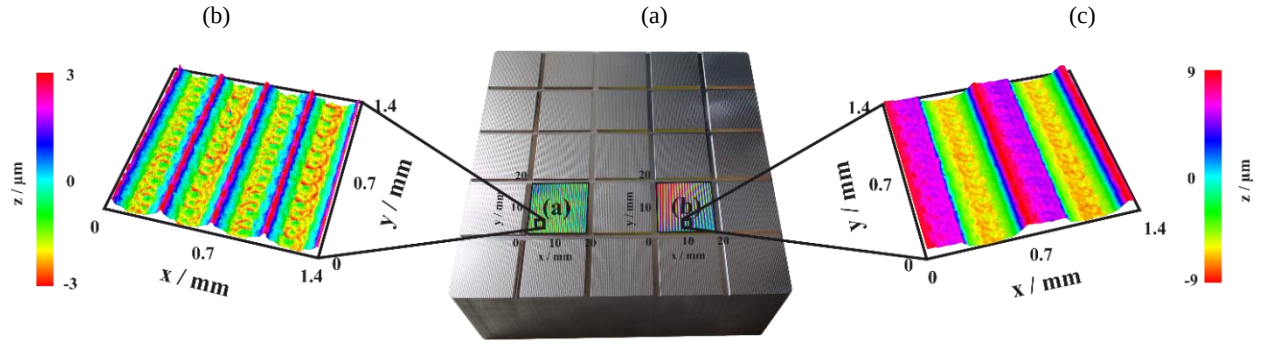

Figure 13. HoloCut measurement data: (a) projected onto exemplary machined sample photograph. (b) detail view of measurement data for good samples F, G in the range of ±3 µm. (c) detail view of measurement data for poor samples H, J in the range of ±9 µm. Milling traces are clearly resolved in both measurements

Figure 14 exemplarily shows the surface parameter *Sq* evaluated with all optical measurement systems previously introduced:

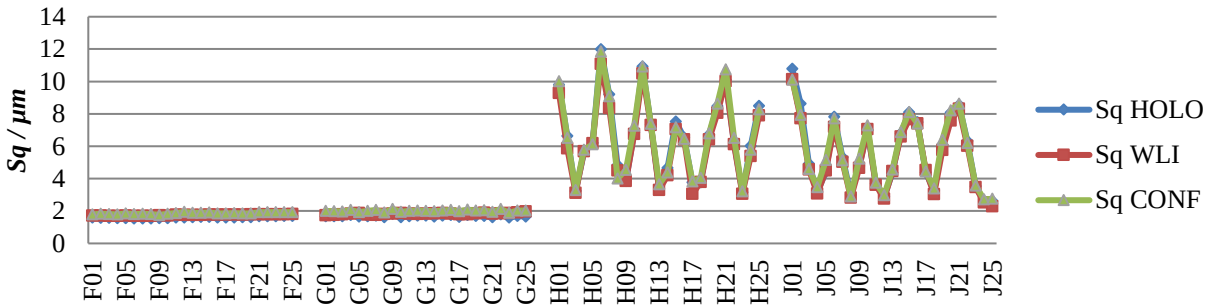

Figure 14. Exemplary surface parameter *Sq* for four samples F, G, H and J measured on HoloCut holographic sensor, Zygo white light interferometer and Nanofocus confocal sensor. Tool malfunction results in strongly fluctuating *Sq* values.

The change in surface roughness between sample F and G compared to H and J by more than one order of magnitude is particularly striking. While the roughness of samples F and G changes in the range of less than 0.5 µm, for samples H and J it is about 9 µm, i.e. 18 times the magnitude. In addition, the measured values of H and J show strong fluctuations among each other. It is assumed that there must have been a significant change in the process conditions. Inspections show, that the calibration data of the HG sensor, which is responsible for sensing the extension of the milling spindle length due to thermal expansion, no longer matched its presets. Consequently, the Z-axis of the milling machine was permanently adjusted in a wrong way. A new calibration of the HG sensor solved the problem. It is remarkable, that the malfunction of the milling machine was detected by all sensors easily even before the machine reported an error. However, with the naked eye, the increase in surface roughness on the samples cannot be detected.

In addition to the obvious differences between samples F and G compared to H and J, Figure 15 shows a zoomed view on samples F and G due to cutter wear. This is manifested in a slight upward trend of the surface roughness *Sq*. On closer analysis, a very good agreement of the qualitative progression of the curves between confocal and holographic sensor can be seen.

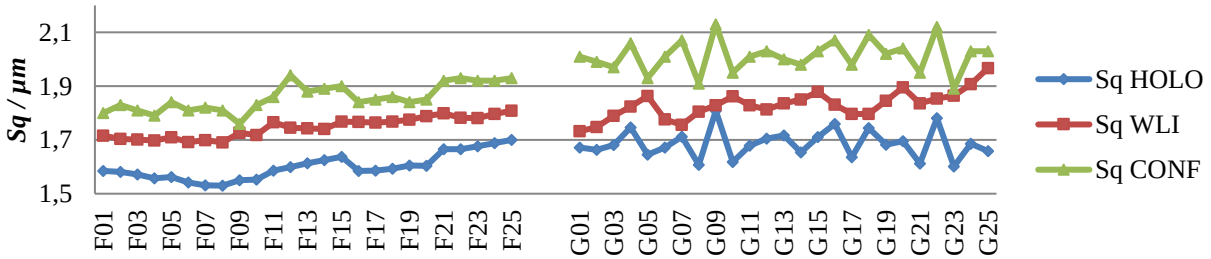

Figure 15. Zoom on samples F and G shows a linear increase of *Sq* which can be attributed to tool wear.

On comparison of the different optical measuring principles, a difference of less than 10 % was observed which is attributed to the different filtering implementations of the optical setups and data-processing approaches. Eventually, it can be stated that the HoloCut sensor is capable of detecting even minor changes in the milling process directly after the respective process steps in the milling machine.

5. CONCLUSION

An optical sensor HoloCut based on multiwavelength digital holography is presented and its application for operation inside machine tools is motivated.

Since multiwavelength digital holography is very susceptible to vibrations, special care has to be taken for operation inside machine tools. Besides mechanical optimizations, an algorithm that allows a prediction of the raw images quality in terms

of vibration is presented along with a solution to correct them if required. In addition to a laboratory proof of design, the algorithm was applied to a measurement of a coin in the machine tool and showed a significant reduction of artefacts. Potential for improvement was identified, which will be incorporated in future investigations.

Furthermore, the surface parameters of ISO 25178 were introduced. The evaluation of these parameters on four equally machined test samples revealed an undetected machine error. For this purpose, the measurement results of the parameter Sq were exemplarily evaluated and compared with reference sensors. It was shown, that the HoloCut sensor is suitable for both qualitative and quantitative evaluation of milled surfaces.

6. ACKNOWLEDGEMENT

This project is financed by Baden-Württemberg Stiftung gGmbH. Production of the sample as well as Zygo white light interferometer evaluations were conducted by Aalen University – Zentrum für Optische Technologien (ZOT). NanoFocus confocal sensor evaluations were carried out by University of Kaiserslautern – Institute for Measurement and Sensor-Technology (mts).

REFERENCES

[1] Carl, D., Fratz, M. and Höfler, H., “Digitale Mehrwellenlängen-Holografie für makroskopische Topografien in mikroskopischer Genauigkeit,‘’ tm - Technisches Messen 77(9), 1–5 (2010).
[2] Speich, M., Börret, R., Rimkus, W. and Harrison, D. K., [Material removal in polishing processes - finite element simulation and experiment] (2012).
[3] Pohl, M. and Börret, R., “Simulation of mid-spatials from the grinding process,‘’ Journal of the European Optical Society - Rapid publications (2016).
[4] Cai, L. Z., Liu, Q. and Yang X. L., “Phase-shift extraction and wave-front reconstruction in phase-shifting interferometry with arbitrary phase steps,‘’ Optics Letters 28(19), 1808–1810 (2003).
[5] Ostrovsky, Y. I., Butusov, M. M. and Ostrovskaya, G. V., [Interferometry by Holography], Springer, Berlin & Heidelberg (1980).
[6] Ostrovsky, Y. I., Shchepinov, V. P. and Yakovlev, V. V., [Holographic Interferometry in Experimental Mechanics], Springer, Berlin & Heidelberg (1991).
[7] Schnars, U. and Juptner, W., “Direct recording of holograms by a CCD target and numerical reconstruction,‘’ Applied Optics 33(2), 179–181 (1994).
[8] Beeck, M.-A. and Hentschel, W., “Laser metrology - a diagnostic tool in automotive development processes,‘’ Optics and Lasers in Engineering 34(2), 101–120 (2000).
[9] Shchepinov, V. P., Pisarev, V. S., Novikov, V. V., Odintsev, I. N. and Bondarenko, M. M., [Strain and stress analysis by holographic and speckle interferometry], Wiley, Chichester (1996).
[10] Kreis, T., [Handbook of holographic interferometry. Optical and digital methods], Wiley-VCH, Weinheim (2005).
[11] Seyler, T., Fratz, M., Beckmann, T., Bertz, A. and Carl, D., “Miniaturized multiwavelength digital holography sensor for extensive in-machine tool measurement,‘’, 103290F.
[12] Carl, D., Fratz, M., Pfeifer, M., Giel, D. M. and Höfler, H., “Multiwavelength digital holography with autocalibration of phase shifts and artificial wavelengths,‘’ Applied Optics 48(34), H1-H8 (2009).
[13] DIN Deutsches Institut für Normung e. V. (12.2016), [Geometrische Produktspezifikation (GPS) - Oberflächenbeschaffenheit: Flächenhaft; Teil 1: Angabe von Oberflächenbeschaffenheit (ISO 25178-1:2016); Deutsche Fassung EN ISO 25178-1:2016] (DIN EN ISO 25178: 12.2016).
[14] DIN Deutsches Institut für Normung e. V. (09.12), [Geometrische Produktspezifikation (GPS) - Oberflächenbeschaffenheit: Flächenhaft; Teil 2: Begriffe und Oberflächen-Kenngrößen (ISO 25178-2:2012); Deutsche Fassung EN ISO 25178-2:2012] (DIN EN ISO 25178: 09.12).
[15] DIN Deutsches Institut für Normung e. V. (11.12), [Geometrische Produktspezifikation (GPS) - Oberflächenbeschaffenheit: Flächenhaft; Teil 3: Spezifikationsoperatoren (ISO 25178-3:2012); Deutsche Fassung EN ISO 25178-3:2012] (DIN EN ISO 25178: 11.12).
[16] Schreier, H., Orteu, J.-J. and Sutton, M. A., [Image Correlation for Shape, Motion and Deformation Measurements], Springer US, Boston, MA (2009).
[17] Pan, B., Qian, K., Xie, H. and Asundi, A., “Two-dimensional digital image correlation for in-plane displacement and strain measurement: a review,‘’ Meas. Sci. Technol. 20(6), 62001 (2009).
[18] Meyer, M., [Signalverarbeitung. Analoge und digitale Signale, Systeme und Filter] (2014).